Quantum calculation of highly excited vibrational energy levels of $CS_2(\tilde{X})$ on a new empirical potential energy surface and semiclassical analysis of 1:2 Fermi resonance

Cheng Zhou [a], Daiqian Xie [a,b], Rongqing Chen [a], Guosen Yan [b], Hua Guo [a], Vivian Tyng [c], Michael E. Kellman [c],*

[a] *Department of Chemistry, University of New Mexico, Albuquerque, NM 87111, USA*
[b] *Department of Chemistry, Sichuan University, Chengdu, Sichuan, PR China*
[c] *Department of Chemistry, University of Oregon, Eugene, OR 97403, USA*

Abstract

We report a refined potential energy function for the ground electronic state of CS_2 based on a least-squares fitting to several low-lying experimental vibrational frequencies. Energy levels up to 20,000 cm^{-1} have been obtained on this empirical potential using the Lanczos algorithm and potential optimized discrete variable representation. Among them, 329 levels below 10,000 cm^{-1} are assigned with approximate normal mode quantum numbers (n_1, n_2^0, n_3), based on expectation values of one-dimensional (1D) reference Hamiltonians. An effective Hamiltonian is extracted from these assigned levels. The agreement with experimental data, including those of several isotopically substituted species, is excellent. In addition, some Fermi and anharmonic resonances are analyzed. The nearest neighbor level spacing and Δ_3 distributions indicated that the vibrational spectrum of CS_2 is largely regular in the energy range up to 20,000 cm^{-1}. Semiclassical phase space analysis, including bifurcation analysis of the spectroscopic Hamiltonian, is used to interpret subtle anomalies signaled by expectation values used in normal mode assignments. The meaning of Fermi resonance is clarified by contrasting the semiclassical analysis of CS_2 and CO_2. © 2002 Published by Elsevier Science B.V.

1. Introduction

The carbon disulfide (CS_2) molecule has been a prototype for studying vibrational and rotational spectra of linear polyatomic molecules. It has a deep ($\sim 36,000$ cm^{-1}) potential well, which is well-separated from electronic excited states [1,2]. A large body of spectroscopic data for various isotopomers has been obtained from a wide range of experimental measurements including diode-laser absorption [3–5], Fourier transform IR [6,7], dispersed fluorescence [8–13], stimulated emission

---

* Corresponding author. Tel.: +1-505-277-1716; fax: +1-505-277-2609.

E-mail address: hguo@unm.edu (H. Guo).

pumping [14–16], and other techniques [17–20]. In particular, we note the recent publications by Pique and co-workers [11,12,21], by Liou and Huang [16], and by Brasen and Demtröder [13], which provide a large number of ro-vibrational levels up to 20,000 cm^{-1}. The analysis of the ro-vibrational levels has led to the determination of anharmonic force fields [22–24], as well as spectroscopic Hamiltonians [3,8,13,16]. Like the extensively studied CO_2 system [25–28], the vibrational spectrum of CS_2 is affected by the 1:2 Fermi resonance between the symmetric stretching and bending modes [29]. As a result, it is sometimes more appropriate to describe the spectrum of a 1:2 resonant system with emphasis on the polyad number $P = n_1 + n_2/2$, as has been recognized for CS_2 [30,31]. Due to the large frequency mismatch between the two modes (658 vs 802 cm^{-1}), however, the Fermi interaction is ineffective in mixing states belonging to the same polyad, at least at low energies [29]. For the highly excited vibrational levels, on the other hand, the aforementioned and other anharmonic resonances make the assignment very difficult. In addition, there has been some discussion on the existence of vibrational chaos [11–13,16,21], which may further complicate the analysis.

Several near-equilibrium potential energy functions have been developed by fitting to low-lying experimentally observed frequencies [32–34] or ab initio data [35]. Variational calculations of the ro-vibrational levels of CS_2 have been reported, but none reached beyond 5000 cm^{-1}. This is in sharp contrast to the wealth of experimental data extending from the zero-point energy to 20,000 cm^{-1}. An accurate theoretical characterization of highly excited vibrational spectrum of polyatomic molecules such as CS_2 is of great importance for a number of reasons. First, it provides valuable information for understanding intermodal coupling, Fermi and anharmonic resonances, large amplitude vibrational dynamics, and ultimately intramolecular vibrational energy redistribution. It is also useful for semiclassical analysis of vibrational dynamics, applied specifically to CS_2 [31], using techniques developed for spectroscopic Hamiltonians used to fit the detailed spectrum [36–40], whether from experiment or from varia-

tional calculations as used here. Second, knowledge of vibrational levels on the ground electronic state helps to elucidate the vibrational structure of the excited electronic states, in the context of emission/Raman spectroscopy [9,41,42]. Also, the theoretical calculation is capable of generating a complete spectrum for the statistical analysis of quantum stochasticity in the vibrational spectrum of this triatomic system.

The major difficulties in a quantum mechanical calculation of the CS_2 ro-vibrational spectrum are the lack of a global potential energy surface (PES) of spectroscopic accuracy and the large number of basis functions (or grid points) needed to converge the energy levels of this relatively massive molecule. Its density of states is a few times higher than its more extensively studied cousin CO_2. Recent progress in the recursive solution of eigenproblems has offered an opportunity to examine the highly excited vibrational spectrum of small polyatomic molecules with reasonable computer power [43–50]. In this work, we report a new empirical PES for $CS_2(\tilde{X}^1\Sigma_g^+)$, constructed from a least-squares fitting to experimental vibrational band origins up to 6000 cm^{-1}. Vibrational energy levels up to 20,000 cm^{-1} are then determined on this PES using the Lanczos method, which relies on recursive matrix-vector multiplication. Combined with the discrete variable representation (DVR) [51], the Lanczos method is capable of extracting relevant eigenvalues of a Hamiltonian matrix with a dimension of a few millions [46,48,50]. Indeed, our calculation reported here can in principle be extended to calculate much higher energy levels, as shown in our recent work [49]. However, uncertainties of the potential energy function at high energies, strong vibrational–rotational coupling, and the possible mixing with low-lying excited electronic state above 23,000 cm^{-1} render such an undertaking less meaningful. This work is organized as follows. The fitting of the PES is briefly discussed in Section 2. The Lanczos method and symmetry adaptation are detailed in Section 3. The results, including properties of the potential, ro-vibrational energy levels for different isotopomers, assignment and the influence of Fermi/anharmonic resonances, are presented and discussed in Section 4. Section 5 concludes.

2. Computation details

2.1. Optimization of the potential energy function

The three-dimensional (3D) potential energy function is expressed as a polynomial expansion ($C_{ijk} = C_{jik}$ due to symmetry):

$$V(r_1 r_2 \theta) = \sum_{ijk} C_{ijk} y_1^i y_2^j y_3^k, \tag{1}$$

where the Morse transformed stretching displacements and the angular displacement are

$$y_1 = 1 - e^{-\alpha_1(r_1 - r_e)},$$
$$y_2 = 1 - e^{-\alpha_2(r_2 - r_e)}, \tag{2}$$
$$y_3 = \cos\theta - \cos\theta_e.$$

Here, r_1 and r_2 are the C–S bond lengths, and θ is the enclosed bond angle. The equilibrium values of the three coordinates were adopted from experimental data: $r_e = 1.5526$ Å and $\theta_e = 180°$ [8]. The use of cosine function ensures the symmetry of the system at the equilibrium. The Morse exponential coefficients were taken from the work of Kolbuszewski et al. [33]. ($\alpha_1 = \alpha_2 = 1.75$ Å^{-1}). This form is expected to be flexible enough to describe the near equilibrium region of the potential, but unlikely to be accurate in the dissociation asymptotes.

The determination of the expansion coefficients was carried out using a least-squares method, which minimizes the following object function:

$$f = \sum_n (E_n^{cal} - E_n^{obs})^2, \tag{3}$$

in which E_n^{obs} are the experimentally determined energy levels and E_n^{cal} are the calculated ones obtained using a variational method [52]. The internal coordinate Hamiltonian [53] was used in the calculation and its eigenvalues and eigenstates were obtained by standard diagonalization. The Hellmann–Feynman theorem was then used to evaluate the derivatives ($\partial f / \partial C_{ijk}$).

2.2. Calculation of highly-excited vibrational levels

The calculation of the highly-excited vibrational levels on the refined PES was carried out using the Lanczos algorithm [54,55], which is based on the following three-term recursion relation:

$$|\psi_{k+1}\rangle = (\hat{H}|\psi_k\rangle - \alpha_k|\psi_k\rangle - \beta_{k-1}|\psi_{k-1}\rangle)/\beta_k,$$
$$k = 1:K. \tag{4}$$

At the kth propagation step, one calculates

$$\alpha_k = \langle\psi_k|\hat{H}|\psi_k\rangle, \tag{5a}$$
$$\beta_k = \|\hat{H}|\psi_k\rangle - \alpha_k|\psi_k\rangle - \beta_{k-1}|\psi_{k-1}\rangle\|,$$
$$\beta_0 = 0. \tag{5b}$$

The above Lanczos algorithm reduces a large Hermitian Hamiltonian matrix ($\hat{H}$) to a smaller real symmetric tridiagonal matrix:

$$[T^{(K)}]_{k',k} = \alpha_k\delta_{k,k'} + \beta_k\delta_{k,k'+1} + \beta_k\delta_{k+1,k'}, \tag{6}$$

which can be readily diagonalized to give approximate eigenvalues of the Hamiltonian. For sufficiently large K, the Lanczos eigenvalues provide a good approximation to all eigenvalues of $\hat{H}$ [55]. As shown in Eq. (4), the major computation in this approach is the matrix-vector ($\hat{H}\psi$) multiplication. Consequently, it has much more favorable scaling laws, which make large systems tractable.

In this work, we use the Radau coordinates (R_1, R_2, χ) because of the simplicity of the kinetic energy operator [56]. For symmetric isotopomers, the problem can be further simplified by symmetrizing the radial coordinates: $R_{\pm} = (R_1 \pm R_2)/\sqrt{2}$. The corresponding Hamiltonian can then be expressed as follows ($\hbar = 1$):

$$\begin{aligned}\hat{H} &= (\hat{T}_+ + V_+) + (\hat{T}_- + V_-) \\ &\quad + [B(R_+, R_-)/B_e](B_e\hat{T}_\chi + V_\chi) \\ &\quad + \{V(R_+, R_-, \chi) - V_+ - V_- \\ &\quad - [B(R_+, R_-)/B_e]V_\chi\} \\ &= \hat{h}_+ + \hat{h}_- + [B(R_+, R_-)/B_e]\hat{h}_\chi + V', \end{aligned} \tag{7}$$

where

$$\hat{T}_{\pm} = -\frac{1}{2m_s}\frac{\partial^2}{\partial R_{\pm}^2}, \tag{8a}$$

$$\hat{T}_\chi = -\frac{1}{\sin\chi}\frac{\partial}{\partial\chi}\left(\sin\chi\frac{\partial}{\partial\chi}\right), \tag{8b}$$

$$B(R_+, R_-) = \frac{2}{m_s} \frac{(R_+^2 + R_-^2)}{(R_+^2 - R_-^2)^2},$$

$$B_e = B(R_+, R_-)\big|_{eq}. \tag{8c}$$

The reference potentials are defined as the 1D cuts of the 3D potential when the remaining two coordinates are fixed at their equilibrium. The Hamiltonian expressed in the above form facilitates the use of the potential-optimized discrete variable representation (PODVR) [57,58]. The PODVR grids were determined by diagonalizing appropriate coordinate matrices spanned by the eigenfunctions of 1D reference Hamiltonians ($\hat{h}$). A 3D direct-product grid was used in evaluating $\hat{H}\psi$ in the Lanczos recursion. The factorizable form of the first three terms in Eq. (7) allows the construction of the Hamiltonian on-the-fly, thus avoiding the storage of the large matrix. The use of partial summation allows a semi-linear scaling for the $\hat{H}\psi$ operation [44,59–61]. The action of the nonseparable potential energy operator was readily accomplished by multiplication in the DVR since $\hat{V}'$ is diagonal on the grid. The convergence of an eigenvalue was ascertained by monitoring the first and last elements of the corresponding Lanczos eigenvector [55,62]. Whenever needed, the eigenfunction can be regenerated by an extra propagation.

A primary reason for using the symmetrized radial Radau coordinates is that the symmetrization of the Hamiltonian and wavepacket can be readily implemented. In particular, only roughly half ($n_-/2$ or $(n_- + 1)/2$ for even and odd n_-) of the wavepacket in the R_- coordinate is needed for each exchange symmetry. The corresponding even/odd 1D reference Hamiltonian matrices ($\hat{h}_-^{e,o}$) are readily constructed as follows:

$$[\hat{h}_-^{e,o}]_{i,j'} = ([\hat{h}_-]_{i,j'} \pm [\hat{h}_-]_{i,n_-+1-i'}),$$

$$i, i' = 1, 2, ..., n_-/2, \tag{9}$$

where the middle point of the grid ($R_- = 0$) is not included in the above symmetrization. Two Lanczos propagations are needed for the two symmetry species. However, the symmetrized scheme is much more efficient because it not only includes half of the original grid, but also significantly reduces the number of propagation steps thanks to the decreased density of states in each species.

The above PODVR form also allows the easy analysis of the vibrational assignment. As illustrated in earlier work [63], the expectation value of a 1D reference Hamiltonian for the entire spectrum can be calculated from an extra Lanczos propagation, with a perturbation proportional to $\hat{h}$. The evaluation of $\hat{h}$ is trivial in direct product PODVR. As such, the assignment of vibrational quantum numbers associated with the degrees of freedom on which the PODVRs are defined can in principle be carried out for all the vibrational levels without the explicit calculation of the wave functions.

3. Numerical results and discussion

3.1. Refined potential energy function and low-lying levels

Low-lying vibrational band origins of CS_2 have been reported by several groups with various precision, due to different experimental techniques used in the measurement. In order to have an unbiased fit, we have used the experimental values ($l = 0$) of Brasen and Demtröder [13]. It has been shown that this spectroscopic Hamiltonian gives a reasonably accurate and balanced representation of the CS_2 vibrational spectrum up to 20,000 cm^{-1}. In this work, only energy levels below 6000 cm^{-1} were included in the fitting. Although there exist more experimental frequencies at higher energies, it becomes difficult to make assignment in the fitting due to the increasing density of states.

The fitting was done with a Hamiltonian in a product finite basis representation [52]. One hundred Legendre polynomials were used for the bending coordinate and 35 1D radial basis function for each of the two stretching coordinates. The latter were obtained by solving the 1D stretching eigen-equation in the region (1.5, 5.0) a_0. Up to 5000 of the lowest basis functions were used in constructing the Hamiltonian matrix. Expansion coefficients in Eq. (1) up to fourth order were fitted using a least-squares method. The initial expansion coefficients were determined from the ab initio force constants of Martin et al. [35].

In practice, the coefficients below the third order were first fitted to energies below 5000 cm^{-1}. The fourth order coefficients were then determined by fitting to all energies below 6000 cm^{-1}, with the lower order coefficients fixed. The final converged result has a root-mean-square (rms) error of 0.20 cm^{-1} for 86 levels included in the fitting. The optimized expansion coefficients are given in the Table 1. The overall agreement between the calculated vibrational energies and those from those spectroscopic Hamiltonian of Brasen and Demtröder is quite satisfactory as the difference seldom exceeds 10 cm^{-1} for levels up to 10,000 cm^{-1}. The refined PES is well-behaved near the equilibrium, as shown by contours in Fig. 1. The force constants of the refined potential are compared in Table 2 with those obtained from experimental and ab initio data. It can be seen that the agreement is also quite satisfactory, particularly at low-orders.

The calculated vibrational ($l = 0$) energies are compared with experimental band origins in Table 3. All calculated energy levels below 5000 cm^{-1} are listed, while only those corresponding to available experimental values are given between 5000 and 10,000 cm^{-1}. These levels are assigned
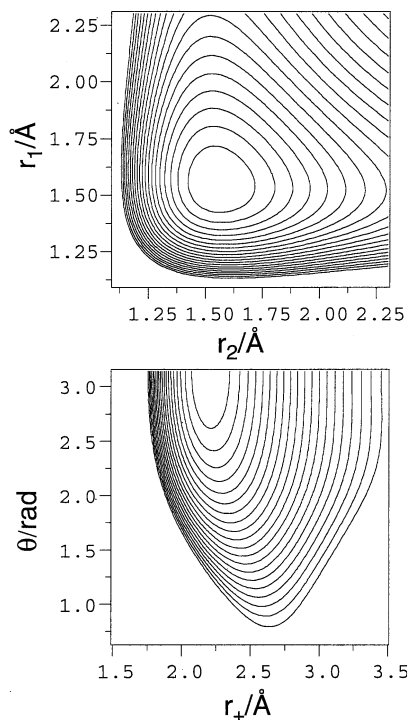

Fig. 1. Contour of the refined potential energy function. Upper panel: the stretch–stretch potential in the two bond-length coordinates (r_1, r_2 at $\theta = 180°$). Lower panel: the stretch–bend potential $r_- = 0$.

with conventional normal mode quantum numbers (n_1, n_2, n_3). As shown below, such assignments are quite reasonable for low-lying levels. The overall agreement between the calculated and observed energies is quite remarkable and rather even in the entire energy range. The largest differences are associated with the low-resolution emission data reported in Ref. [10]. Energy levels with $l = 1$ have also been calculated up to 4000 cm^{-1} and listed in Table 4. Although none of the levels were included in the fitting, the agreement between the calculated and observed values is quite good throughout the energy range. This lends further support to the reliability of the refined potential.

Experimental vibrational frequencies have been reported for a number of isotopomers of CS_2. In order to examine the suitability of our potential for heavier carbon disulfides, we have computed vibrational energy levels up to 4000 cm^{-1} for

Table 1
Expansion coefficients of the refined potential energy function

i	j	k	C_{ijk} (cm^{-1})
0	0	1	28646.6842
0	0	2	13690.3840
1	0	1	−21015.4410
1	1	0	10568.1750
2	0	0	64740.8474
0	0	3	9468.89921
1	0	2	−13073.4584
1	1	1	18598.0445
2	0	1	−7131.57823
2	1	0	−2556.00644
3	0	0	−5004.25190
1	0	3	−11661.5846
1	1	2	22405.6539
2	0	2	19863.5620
2	1	1	4833.18830
2	2	0	−101.829156
3	0	1	−8409.28223
3	1	0	707.741471
4	0	0	454.792439

several isotopically substituted species. As shown in Table 4, the level of agreement with available experimental data is consistent with the normal isotope. These results indicate that the effect of isotope substitution on the potential is relatively insignificant (Table 5).

The vibrational energy levels ($l = 0$) listed in Table 3 were used to determine spectroscopic constants of an effective Hamiltonian using a least-squares method [13,19]. The diagonal element of the effective Hamiltonian are expressed as a Dunham expansion:

$$\langle n_1, n_2', n_3 |H| n_1, n_2', n_3 \rangle$$

$$= \sum_i \omega_i \left(n_i + \frac{d_i}{2} \right) + \sum_{i \leq j} x_{ij} \left(n_i + \frac{d_i}{2} \right) \left(n_j + \frac{d_j}{2} \right)$$

$$+ y_{111} \left(n_1 + \frac{1}{2} \right)^3 + y_{222}(n_2 + 1)^3$$

$$+ y_{333} \left(n_3 + \frac{1}{2} \right)^3 + g_{22}l^2. \tag{10}$$

where d_i denotes the degeneracy. The off-diagonal elements due to the 1:2 Fermi resonance are given as below:

$$\langle n_1, n_2', n_3 |H| n_1 + 1, (n_2 - 2)', n_3 \rangle$$

$$= \frac{1}{2} \sqrt{n_1[(n_2 + 2)^2 - l^2]} \tag{11}$$

$$\left[-\frac{k_{122}}{\sqrt{2}} + \lambda_1 n_1 + \lambda_2(n_2 + 2) + \lambda_3 \left(n_3 + \frac{1}{2} \right) \right.$$

$$+ \lambda_{12} n_1 (n_2 + 2)$$

$$\left. + \lambda_{13} n_1 \left(n_3 + \frac{1}{2} \right) + \lambda_{23}(n_2 + 2) \left(n_3 + \frac{1}{2} \right) + \gamma l^2 \right].$$

This effective Hamiltonian describes the calculated energy levels very well, the rms error is 0.08 cm^{-1} for $l = 0$ levels. The parameters are compared in Table 6 with those obtained from experimental measurements. The harmonic frequencies (ω_i), first anharmonicities (x_{ij}) and the Fermi coupling constant (k_{122}) are all in excellent agreement with experimental data.

3.2. Highly excited vibrational levels

Highly excited energy vibrational levels of CS_2 up to 20,000 cm^{-1} have been determined using the Lanczos algorithm. The system can be accurately represented by $70 \times 40 \times 50$ PODVR grid in the symmetrized Radau coordinates (R_+, R_-, χ) (note that only half of the R_- grid was used in each symmetry-adapted propagation). The basis convergence was ascertained by comparing with results obtained from a smaller grid. The potential cutoff was at 50,000 cm^{-1}, which, combining with the PODVR energy cutoffs, gave a spectral range of $\sim 177,000$ cm^{-1}. The convergence with regard to the propagation steps was also checked by the smallness of the last element of the corresponding Lanczos eigenvector [55], calculated using a modified QL method [64]. It was found that 4000 steps were sufficient for energy levels up to 20,000 cm^{-1} above the zero point energy. Only energy levels with zero vibrational angular momentum ($l = 0$) were calculated.

A total of 2339 vibrational levels were found below 20,000 cm^{-1}, among which 1283 (1056) levels are (anti-)symmetric with respect to the exchange of the two C–S bonds. The complete list of the energy levels can be obtained from the corresponding author. Fig. 2 displays the number of levels up to energy E (the staircase function $N(E)$) for the even species. This function can be readily fitted by a third-order poly-

Table 2
Comparison of the quartic force fields in internal coordinates of CS_2

Force constants	This work	Ab initio [35]	Exp. [22]
f_{rr}	7.87731	7.77669	7.8808
$f_{rr'}$	0.64292	0.56792	0.6472
$f_{\theta\theta}$	0.56906	0.57839	0.5698
f_{rrr}	−44.5515	−43.66658	−44.0946
$f_{rrr'}$	−2.79447	−1.009687	−1.01
$f_{r\theta\theta}$	−0.73057	−0.73804	−0.7396
f_{rrrr}	204.464	195.53266	181.704
$f_{rrrr'}$	7.58632	1.85889	−8.9604
$f_{rrr'r'}$	2.84549	1.23631	−6.984
$f_{rr\theta\theta}$	0.41078	0.77225	1.0876
$f_{rr'\theta\theta}$	1.13143	1.65808	1.5910
$f_{\theta\theta\theta\theta}$	1.06268	4.43938	0.8112

Units are aJ, Å, and Radian.

Table 3
Comparison of the calculated and observed energy levels (cm^{-1}) of CS$_2$ ($l = 0$)

n_1	n_2	n_3	E^{cal}	E^{obs}	Ref.	n_1	n_2	n_3	E^{cal}	E^{obs}	Ref.	n_1	n_2	n_3	E^{cal}	E^{obs}	Ref.
1	0	0	658.048	658.00	a	1	6	1	4567.27	4566.81	c	5	10	0	7197.98	7196.9	b
0	2	0	801.900	801.3	b	0	4	2	4627.11	4627	d	1	16	0	7324.59	7324.1	b
2	0	0	1313.82	1313.70	c	6	2	0	4647.40	–	–	4	12	0	7419.37	7418.8	b
1	2	0	1447.21	1447.4	b	1	10	0	4752.81	4750.2	b	2	8	2	7455.96	7454.3	b
0	0	1	1535.45	1535.35	c	5	0	1	4761.33	–	–	0	18	0	7607.14	7608.8	b
0	4	0	1619.82	1619.78	c	0	8	1	4776.04	–	–	7	8	0	7611.45	7609	e
3	0	0	1967.22	1966.97	c	5	4	0	4783.73	4781	d	3	14	0	7659.69	7661	e
2	2	0	2090.67	2094	d	4	2	1	4863.01	–	–	1	10	2	7670.66	7669.5	b
1	0	1	2185.60	2185.47	c	4	6	0	4952.68	4950.9	b	6	10	0	7807.59	7806.5	b
1	4	0	2255.45	2254.70	b	3	0	2	4977.22	4971.3	b	0	12	2	7906.17	7905.0	b
0	2	1	2324.57	2324.55	c	0	12	0	4997.14	4998	e	2	16	0	7917.99	7918.7	b
0	6	0	2450.09	2450.05	c	2	2	2	5091.12	5087	d	5	12	0	8023.93	8020.7	b
4	0	0	2618.11	2616	d	3	8	0	5147.55	5149	e	3	8	2	8058.39	8057.5	b
3	2	0	2732.32	2727	d	1	0	3	5201.60	5201.15	c	1	18	0	8194.00	8194.1	b
2	0	1	2833.41	2833.19	c	1	4	2	5246.88	5247	d	8	8	0	8225.25	8224	e
2	4	0	2889.62	2889.7	b	7	2	0	5282.84	5282	d	4	14	0	8258.90	8261	e
1	2	1	2961.91	2961.76	c	0	2	3	5330.82	5330.78	c	2	10	2	8267.31	8265.7	b
0	0	2	3057.84	3057.63	c	2	10	0	5365.02	5362.9	b	7	10	0	8416.62	8415.6	b
1	6	0	3077.42	3077.4	b	6	4	0	5412.45	5413	e	1	12	2	8496.71	8496.5	b
0	4	1	3129.96	3129.98	c	0	6	2	5432.63	5431.8	b	0	20	0	8487.90	8486.4	b
5	0	0	3266.31	3269	d	5	6	0	5575.56	5573.2	b	3	16	0	8511.64	8512.5	b
0	8	0	3290.63	3291.20	b	1	12	0	5603.24	5602.9	b	6	12	0	8628.00	8627.9	b
4	2	0	3372.25	–	–	4	0	2	5611.73	5611	d	0	14	2	8745.88	8744.8	b
3	0	1	3478.74	3478.39	c	3	2	2	5716.84	5714	d	2	18	0	8781.30	8782.2	b
3	4	0	3522.37	–	–	4	8	0	5764.81	5765	e	9	8	0	8838.19	8833	e
2	2	1	3597.38	3597.04	c	0	14	0	5861.16	5860.6	b	5	14	0	8857.82	8858.8	b
1	0	2	3700.11	–	–	2	4	2	5865.18	5862	d	8	10	0	9024.94	9024	e
2	6	0	3703.62	3703.2	b	8	2	0	5916.97	5914	d	1	20	0	9068.33	9068.3	b
1	4	1	3757.65	3757.47	c	3	10	0	5976.64	5977	e	2	12	2	9087.04	9085.5	b
0	2	2	3834.20	3832	d	7	4	0	6039.94	6037	d	4	16	0	9105.34	9107.0	b
1	8	0	3910.45	3910.8	b	1	6	2	6044.17	6043	d	7	12	0	9231.57	9232	e
6	0	0	3911.65	–	–	0	0	4	6063.54	6061	d	1	14	2	9329.98	9327.1	b
0	6	1	3947.83	–	–	6	6	0	6197.36	6198	e	3	18	0	9367.95	9370	e
5	2	0	4010.57	–	–	2	12	0	6209.03	6208.7	b	0	22	0	9374.52	9372.7	b
4	0	1	4121.44	–	–	5	4	1	6254.12	6248.2	b	6	14	0	9456.35	9456.4	b
0	10	0	4140.01	4141	d	5	8	0	6381.22	6380.1	b	9	10	0	9632.62	9630.3	b
4	4	0	4153.72	4153.7	b	1	14	0	6460.77	6460.5	b	2	20	0	9649.49	9651.3	b
3	2	1	4231.05	–	–	3	4	2	6482.06	6481	d	3	12	2	9676.63	9675.0	b
3	6	0	4328.70	4328	e	4	10	0	6587.63	6588	e	5	16	0	9699.02	9700.2	b
2	0	2	4339.95	4335	d	0	16	0	6731.37	6730.6	b	7	10	1	9834.81	9834.1	b
2	4	1	4383.87	–	–	3	12	0	6814.29	6813.8	b	2	14	2	9913.96	9912.5	b
1	2	2	4463.60	4465	d	1	8	2	6852.68	6851.3	b	1	22	0	9946.03	9945	e
2	8	0	4529.42	4526.6	b	6	8	0	6996.77	6995.6	b	4	18	0	9958.55	9960.9	b
7	0	0	4553.90	–	–	2	14	0	7060.29	7058.2	b						
0	0	3	4567.17	–	–	0	10	2	7073.46	7072.4	b						

a: Ref. [17]; b: Ref. [13]; c: Ref. [3]; d: Ref. [10]; e: Ref. [11].

nomial, consistent with the three degrees of freedom of the system [65]. We found no evidence of a transition from a E^2 dependence to a E^3 one, as reported by Sitja and Pique [12]. The reported transition is later attributed to pumping contamination [21].

3.3. Quantum stochasticity

There has been some controversy over the experimental 'detection' of the vibrational chaos in CS_2. Pique and co-workers earlier presented evidence of a regular-to-chaotic transition near 12,000 cm^{-1} [11,12,30]. However, it was later suggested that an impure excitation was responsible for the 'chaotic' behavior of the spectrum [21]. The recent work by Brasen and Demtröder found no sign of chaos in the CS_2 vibrational spectrum [13]. On the other hand, Liou and Huang have observed significant irregularities above 12,000 cm^{-1} in their two-dimensional (2D) trajectory study [16]. We focus here on two statistical measures of the spectral fluctuation [66,67]. The nearest neighbor level spacing (NNLS) distribu-

Table 4
Comparison of the calculated and observed energy levels (cm^{-1}) of CS_2 ($l = 1$)

n_1	n_2	n_3	E^{cal}	E^{obs}	Ref.
0	1	0	396.25	396.10	a
1	1	0	1046.80	1046.67	b
0	3	0	1207.17	1206.10	b
2	1	0	1695.06	1694.87	b
1	3	0	1847.16	1846.94	b
0	1	1	1925.19	1925.10	b
0	5	0	2031.83	2031.74	b
3	1	0	2340.94		
2	3	0	2485.44		
1	1	1	2567.73	2567.54	b
1	5	0	2663.03		
0	3	1	2723.52	2723.47	b
0	7	0	2867.62		
4	1	0	2984.35		
3	3	0	3122.04		
2	1	1	3207.89	3207.55	b
2	5	0	3292.92		
1	3	1	3355.52	3355.30	b
0	1	2	3441.06		
1	7	0	3491.01		
0	5	1	3535.73	3534	c
5	1	0	3625.23		
0	9	0	3712.87		
4	3	0	3756.99		
3	1	1	3845.60		
3	5	0	3921.51		
2	3	1	3985.81		

a: Ref. [16]; b: Ref. [3]; c: Ref. [11].

tion provides information on the short range level repulsion [68,69]. The Δ_3 distribution, which is the ensemble averaged least-squares deviation of the number of levels from a straight line, is an indicator of the long range correlation [70].

To calculate these two distributions, the spectrum was first unfolded to remove the secular contributions [71]. As the insert in Fig. 2 suggests, the unfolded energy spectrum provides an unbiased averaged level density throughout the spectral range. The NNLS distribution of the unfolded levels with even exchange symmetry is plotted in the upper panel of Fig. 3 as a function of the level separation (s). The Wigner and Poisson distributions plotted in the same figure correspond, respectively to the chaotic and regular limits. It is clear that the CS_2 vibrational spectrum can be reasonably well described by the Poisson distribution, although some nearest neighbor level repulsion does exist. The level repulsion is presumably due to the state mixing by intermodal interactions, particularly at high energies. This short range regularity is supported by the long range Δ_3 distribution, which is shown in the lower panel of the same figure. At small r (average number of levels), the Δ_3 distribution follows closely the line characterizing a regular system, rather than the curve in the Gaussian orthogonal ensemble (GOE) limit. It eventually levels off due to the saturation effect [69]. Overall, our results indicate that the presence of the vibrational irregularity is limited in CS_2, consistent with the conclusion reached recently by several experimental groups [13,21]. However, as will be seen below, at the level of spectroscopic assignment, CS_2 definitely shows effects of irregularities due to anharmonic resonances which are subtle but nonetheless can be interpreted in detail.

3.4. Vibrational assignment and Fermi resonance

The assignment of vibrational quantum numbers to a large number of levels can be a daunting task if one relies on the inspection of the corresponding wave functions. In this work, we attempt to carry out the assignment in terms of the expectations values of three 1D reference Hamil-

Table 5
Comparison of the calculated and observed vibrational energy levels (in cm^{-1}) for three isotopomers of CS_2

n_1	n_2	n_3	$^{13}CS_2$			$^{34}SC^{32}S$			$^{33}SC^{32}S$		
			E^{cal}	E^{obs}	Ref.	E^{cal}	E^{obs}	Ref.	E^{cal}	E^{obs}	Ref.
1	0	0	657.289	657.24	a	648.658	648.37	b	653.243		
0	2	0	776.583	776.55	a	799.627			800.726		
2	0	0	1311.95	1311.80	a	1295.20			1304.30		
1	2	0	1421.08	1420.93	a	1435.91			1441.41		
0	0	1	1485.44	1485.33	a	1532.00	1531.89	c	1533.67	1533.57	c
0	4	0	1569.29	1596.22	a	1614.85			1617.25		
3	0	0	1963.76	1963.47	a	1939.55			1953.07		
2	2	0	2063.65			2070.43			2080.30		
1	0	1	2135.02	2134.86	a	2172.92	2172.77	b	2179.10	2178.95	d
1	4	0	2204.35			2241.59			2248.34		
0	2	1	2250.18	2250.13	a	2318.86			2321.62		
0	6	0	2374.04			2442.24			2446.04		
4	0	0	2612.40			2581.62			2599.46		
3	2	0	2704.43			2703.22			2717.41		
2	0	1	2781.86	2781.61	a	2811.66			2822.27		
2	4	0	2837.88			2866.96			2878.00		
1	2	1	2886.95	2886.78	a	2947.32			2954.42		
0	0	2	2958.70	2958.47	a	3050.97			3054.30		
1	6	0	3001.12			3060.77			3068.86		
0	4	1	3031.26			3121.58			3125.63		
0	8	0	3188.69			3221.29			3243.32		
5	0	0	3257.52			3279.81			3285.05		
4	2	0	3343.62			3334.33			3352.83		
3	0	1	3425.71	3425.30	a	3448.13			3463.07		
3	4	0	3469.92			3490.96			3506.27		
2	2	1	3521.81	3521.45	a	3574.00			3585.39		
1	0	2	3600.58			3678.23			3690.59		
2	6	0	3626.96			3684.18			3691.93		
1	4	1	3658.64			3740.52			3748.84		
0	2	2	3711.63			3825.09			3829.50		
1	8	0	3808.61			3858.51			3884.57		
0	6	1	3824.47			3890.87			3900.38		
6	0	0	3898.73			3936.59			3942.03		
5	2	0	3891.39			3963.89			3986.68		

a: [5]; b: [23]; c: [4]; d: [18].

tonians. As mentioned above, these expectation values can be readily obtained in PODVR by additional Lanczos propagations with $\hat{h}$ added as a perturbation term [63]. In particular, the 1D reference potential was chosen as the cut of the 3D potential with the other two coordinates fixed at their equilibrium values. The symmetrized Radau coordinates are a good representation of the three normal modes near the equilibrium geometry. This is evidenced by the fact that the fundamenal frequencies of the three 1D systems (671, 809, 1570 cm^{-1}) are very close to the corresponding 3D ones (658, 802, and 1536 cm^{-1}).

Fig. 4 displays the expectation value of the anti-symmetric stretching mode reference Hamiltonian, $\langle \hat{h}_- \rangle$, for the even exchange symmetry. Most levels, particularly the low-energy ones, have one of several quantized $\langle \hat{h}_- \rangle$ values with an interval of ~ 3100 cm^{-1}. The even n_3 is due to the symmetry in exchanging the two C–S bond. It is quite obvious that the antisymmetric stretch is largely decoupled from the other two vibrational

modes. Consequently, the assignment of n_3 can be made unambiguously for most levels below 12,000 cm^{-1}, consistent with experimental observations [11,12]. At higher energies, however, the assignment becomes difficult due to mixing of states by anharmonic resonances. We will have more to say about assignment in the presence of these resonances in the semiclassical analysis in Section 3.6.

Now we concentrate on the vibrational levels corresponding to $n_3 = 0$. Fig. 5 plots the expectation values for the symmetric stretching and bending modes, $\langle \hat{h}_+ \rangle$ and $\langle \hat{h}_\chi \rangle$, below 15,000 cm^{-1}. The regularity in these plots is quite apparent, particularly for levels below 10,000 cm^{-1}. Due to the strong coupling between these two coordinates, these expectation values do not fall in straight lines, as in the case of $\langle \hat{h}_- \rangle$. However, it is not difficult to identify the corresponding normal mode quantum numbers. In the upper panel, for example, one can assign the bottom points to the $(0, n_2, 0)$ progression; and the top points to the $(n_1, 0, 0)$. From these expectation values, 329 energy levels with zero vibrational angular momentum $(l = 0)$ below 10,000 cm^{-1} have been assigned with the three normal mode quantum numbers. Some of them are listed in Table 3. The

Table 6
Parameters for the effective Hamiltonian (in cm^{-1})

	This work	Exp. [16]	Exp. [13]
ω_1	671.942	672.276	672.848
ω_2	398.262	398.019	398.099
ω_3	1558.939	1558.680	1558.787
x_{11}	−0.849470	−0.981	−1.028600
x_{12}	−3.296208	−2.952	−3.150430
x_{13}	−7.532798	−7.669	−7.648050
x_{22}	1.252846	1.218	1.212950
x_{23}	−6.479642	−6.453	−6.445290
x_{33}	−6.669706	−6.536	−6.534490
y_{111}	−0.004572		−0.000939
y_{222}	−0.006890	−0.00637	−0.005297
y_{333}	0.023238		−0.002108
k_{122}	39.818659	41.369	41.476040
λ_1	0.311117		0.493641
λ_2	0.413486		0.459236
λ_3	−0.128042		−0.050351
λ_{12}	0.012359		0.005724
λ_{13}	−0.019593		−0.002625
λ_{23}	−0.003142		0.001455

complete list of assigned energy levels can be obtained from the corresponding author.

From the same figures, one can further identify the polyad number $P = n_1 + n_2/2$ and the corresponding members. Indeed, the $\langle \hat{h}_+ \rangle + \langle \hat{h}_\chi \rangle$ values are quite similar for members of the same polyad (note that only even n_2 are allowed because $l = 0$). In Fig. 6, the wave functions of the $P = 9$ family are plotted in the $(\cos \chi$ and $R_+)$ coordinates. The stretch-bend coupling is quite obvious from these skewed shaped wave functions. It is apparent that all the wave functions possess clear nodal structures. The nodal planes are rather curved due to the coupling, but not nearly so much as the case of CO_2 and other Fermi resonance systems [72]. This does not, however, mean that the coupling among the levels of CS_2 is weak. To understand this paradox, we recall that a simple two-state perturbation theory attributes the mixing of two near degenerate states to the coupling matrix element as well as the energy gap. Although the coupling constant for the 1:2 Fermi resonance is not small (40 cm^{-1}) for CS_2, the relatively large frequency mismatch between the two modes (658 vs 802 cm^{-1}) renders the intra-polyad mixing rather inefficient. We will have much more to say about the detailed state-by-state manifestations of the Fermi resonance, and also about the contrast with the strongly resonant CO_2, in the semiclassical analysis in Section 3.6.

The increasing level density at higher energies makes state mixing more frequent. For example, it can be seen from Fig. 3 that there are four pairs of levels with $\langle \hat{h}_- \rangle$ values between 0 and 3000 cm^{-1}, as highlighted as filled cycles. The lower members are also highlighted in Fig. 4 and they exhibit notable deviations from the regular pattern. The deviation from the quantized expectation values indicates significant state mixing. The identity of these pairs can be determined from Figs. 3 and 4 as $(5, 14, 0)/(3, 12, 2)$, $(6, 14, 0)/(4, 12, 2)$, $(7, 14, 0)/(5, 12, 2)$, and $(8, 14, 0)/(6, 12, 2)$, near 8858, 9456, 10,056 and 10,653 cm^{-1}, respectively. Apparently, such three-mode anharmonic resonances depend on a higher order coupling term than the intra-polyad 1:2 Fermi resonance. However, the former is amplified by the small energy gaps, tuned by the increasing n_1.
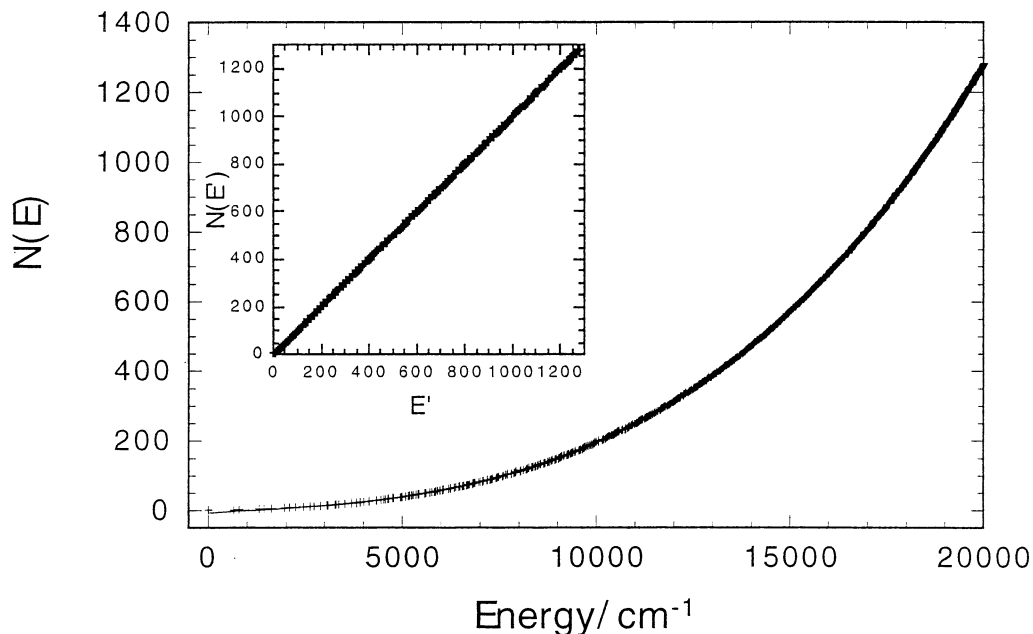
Fig. 2. Staircase function of the even CS_2 energy levels as a function of the energy, with the third-order polynomial fit represented by a line. The insert displays the staircase function as a function of the unfolded energy (E').

Similar mixing of states becomes much more prevalent above 12,000 cm^{-1}, which leads to the destruction of the regular structure in Fig. 4. It should however be stressed that the calculated results presented here are not expected to be spectroscopically accurate. Since state mixing depends sensitively on the energies, it is not realistic to compare them with experimental data.

3.5. Anomalies of the normal mode assignments

The lower energy states plotted in Fig. 5 fall into clear polyad 'bands', especially below 10,000 cm^{-1}, and the analysis in terms of symmetric stretch and bend content is fairly consistent with a conventional normal mode assignment in terms of quantum numbers (n_1, n_2^0, n_3). Nonetheless, there are some evident irregularities within the polyads, even when the polyads themselves are quite distinct. We have already considered the four states labeled with black filled symbols in Figs. 4 and 5, associated with breaking of the n_3 quantum number. Another irregularity appears starting at about polyad $P = 8$ or 9. A 'kink' is evident at the

top of the polyad, where the states take the maximal value of the symmetric stretch quantum number n_1. For $P = 9$, there are two states with almost the same expectation value of the symmetric stretch, indicating that n_1 and n_2 cannot truly be approximate integer quantum numbers. The kink persists to higher P.

Another anomaly is seen in Fig. 6. The maximum or 'ridge' of the wave function for the state assigned $(9, 0, 0)$ does not fall along the pure symmetric stretch coordinate R_+, but rather has apparent bend character. The ridge of the full wave function, with the bend coordinate reflected across the $\cos \chi = -1$ plane, has a 'hairpin' shape. In contrast, for lower values of P, the ridge falls clearly along the symmetric stretch. Recall from Fig. 5 that $P = 9$ is also where the kink in $\langle \hat{h}_+ \rangle$ and $\langle \hat{h}_\chi \rangle$ sets in, for the same state $(9, 0, 0)$. We will present an explanation in Section 3.6 of these anomalies in the patterns of Figs. 5 and 6 in terms of a semiclassical phase space analysis of the spectroscopic Hamiltonian.

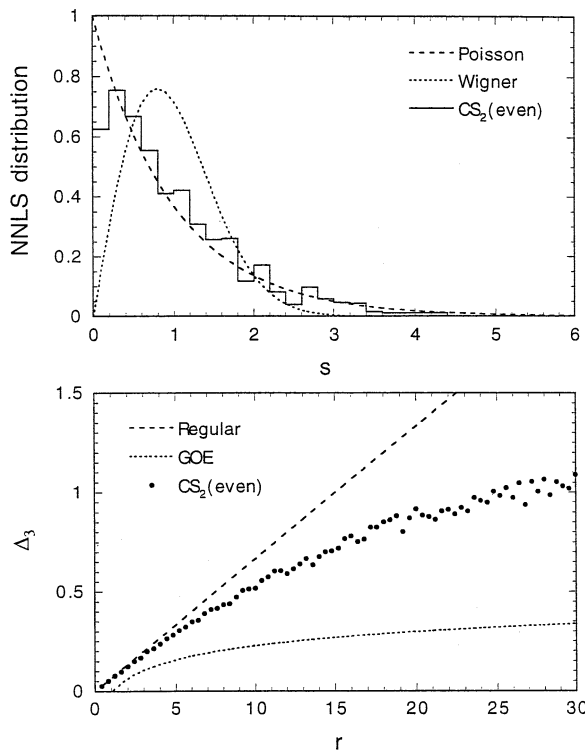Eventually, a region is reached in Fig. 5 where the polyad bands are no longer distinct, indicating

Fig. 3. Nearest neighbor level spacing and Δ_3 distributions for the even CS_2 energy levels below 20,000 cm^{-1}.

polyad mixing with the breakdown of the polyad number. This happens at approximately the same energy ($\sim 12{,}000$ cm^{-1}) where widespread breakdown of the n_3 quantum number is evident in Fig. 4. The phenomena are the same: the polyad num-
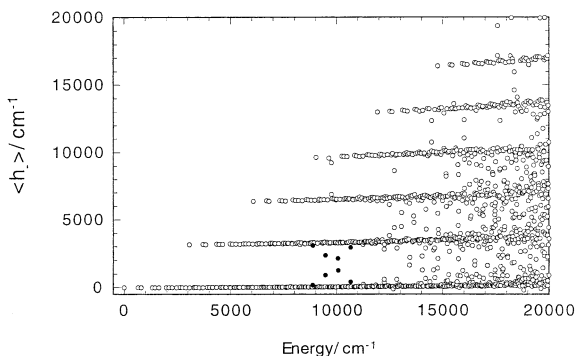

Fig. 4. Expectation values $\langle \hat{h}_- \rangle$ for the even CS_2 energy levels up to 20,000 cm^{-1}. The filled cycles denote the resonances discussed in text.
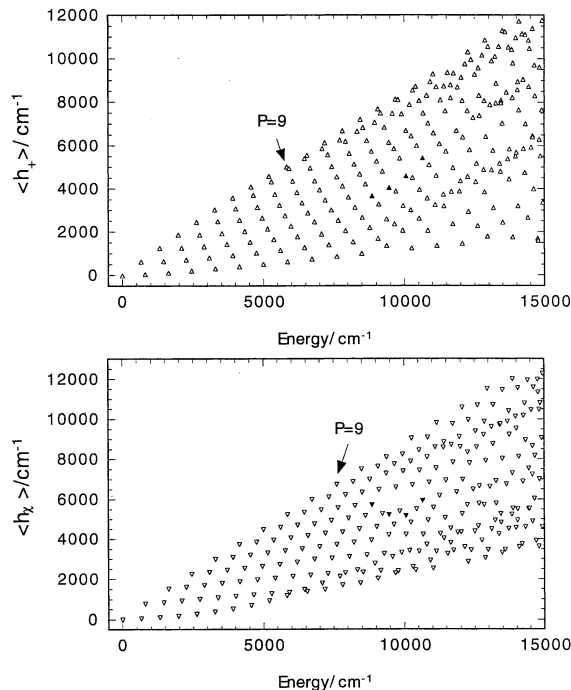
Fig. 5. Expectation values $\langle \hat{h}_+ \rangle$ and $\langle \hat{h}_\chi \rangle$ for the even CS_2 energy levels up to 20,000 cm^{-1}. The filled triangles denote the resonances discussed in text.

ber $P = n_1 + n_2/2$ is broken by resonances which mix in states with different n_3. The emergence of multiple important resonances, in addition to the 1:2 Fermi resonance that dominates at lower energy, signals the onset of significant chaos. We will not have much to say about this in terms of semiclassical analysis, because the effective single resonance Hamiltonian used here is not general enough for a quantitative account of this disordered, multiresonant spectral region. However, methods are now available [73–75] for classifying patterns of spectra which are significantly influenced by chaos, when a multiresonance effective Hamiltonian is available.

3.6. Semiclassical phase space analysis

To understand the patterns in Figs. 4–6, we make use of tools of nonlinear dynamics developed for analysis of vibrational spectra. The motivation for these dynamical methods is that in highly excited states, the internal motions of
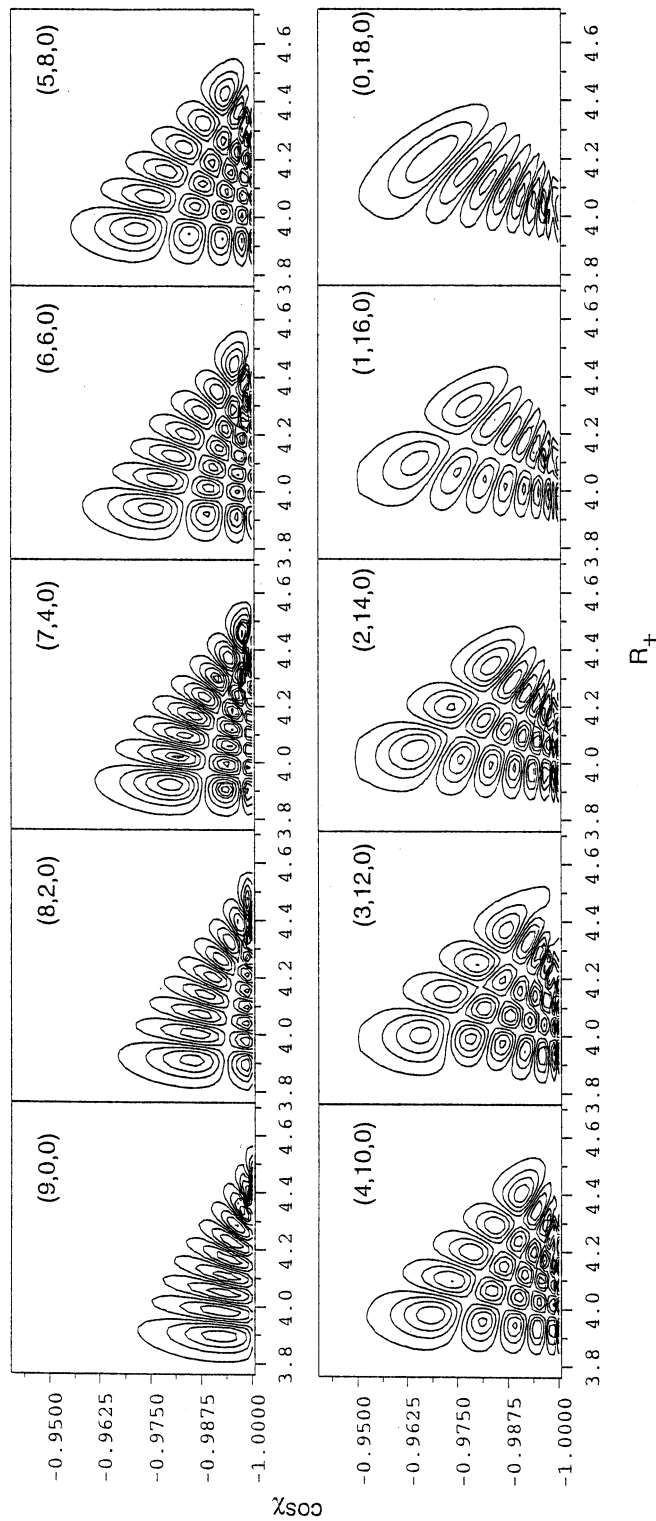
Fig. 6. Contours of the wave functions belonging to the $P = 9$ polyad family. ($R_- = 0$).

molecules change in a fundamental way from the standard low-energy normal modes. Several didactic reviews of these new methods are available [76–78]. The tools used in this paper include a semiclassical phase space representation of spectra called the polyad phase sphere, and analysis of bifurcations of the low-energy normal modes.

The phase sphere is a way of representing and visualizing the vibrational spectrum. In molecular vibrational problems, the phase sphere was first developed for a system of two coupled stretch modes exhibiting the transition from normal to local modes [37]. Formally, this is equivalent to the construct familiar in physics as the Bloch sphere, which has ubiquitous applications, for example, in Bose–Einstein condensates [79]. In molecular problems, the phase sphere has been generalized [38] to systems with Fermi resonance, e.g. the 1:2 resonance treated here. Review presentations can be found in Refs. [77,78].

Each polyad is represented by a separate sphere. On a given polyad sphere, each level of the polyad is represented by a semiclassical trajectory. The phase spheres are computed using a well-defined procedure [37] from the spectroscopic Hamiltonian with its parameters optimized to fit the spectrum, in the present case, those in Table 6.

Fig. 7 shows the sphere for polyad $P = 12$. The effects of the Fermi resonance coupling are clearly evident. If there were only diagonal, zero-order contributions to the Hamiltonian, the quantum energy levels would be represented by regular azimuthal circles, like the latitudinal parallels on a globe of the earth, circling around the north and south poles (which represent, respectively the pure symmetric stretching and bending overtones of the polyad). Instead, Fig. 7 shows that the flow lines are 'off-axis', with a distinct 'marbled' appearance at the top.

This accounts, as follows, for the kink at the top of the polyad 12 band in Fig. 5 (top) and at the bottom of the polyad 12 band in Fig. 5 (bottom). Trajectory 2 (second lowest in energy) in Fig. 7 goes almost right through the north pole (pure symmetric stretch), and plausibly has more symmetric stretching character than trajectory 1. Consistent with this, in Fig. 5, level 2 has the maximal value of $\langle \hat{h}_+ \rangle$ (top panel) and minimal

value of $\langle \hat{h}_\chi \rangle$. We have analyzed this correspondence quantitatively with the phase sphere by computing the symmetric stretching energy as an expectation value $\langle \hat{h}_s \rangle$ for each eigenvector from the fit:

$$\langle \hat{h}_s \rangle = \langle \omega_1 n_1 + x_{11} n_1^2 + y_{111} n_1^3 \rangle. \tag{12}$$

The results, shown in Fig. 8, confirm our interpretation. The overall similarity is evident between Figs. 8 and 5 (top), the latter being from the ab initio wave functions. (The reasons for the differences between the two figures—mainly, the greater simplicity of Fig. 8—will be discussed later, but it is worth remembering that Fig. 8 comes from a fit of only a part of the spectrum with a very simple, single Fermi resonance effective Hamiltonian.)

Next, we interpret the 'marbled' appearance of the sphere in Fig. 7 in terms of bifurcation analysis. The interplay of anharmonicity and the Fermi resonance coupling in the spectroscopic Hamiltonian gives rise to bifurcations of the normal modes. In a bifurcation, a normal mode abruptly branches into new anharmonic modes. The best-
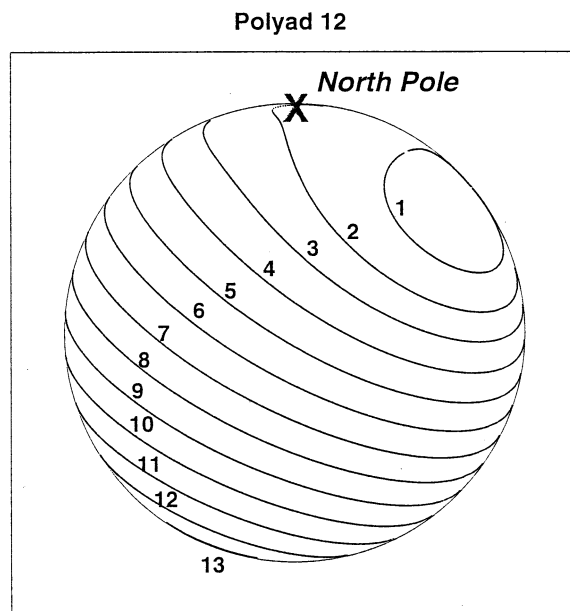
Polyad 12

Fig. 7. Polyad phase sphere for polyad $P = 12$ CS_2. The contour lines correspond semiclassically to levels of the polyad, numbered in order of increasing energy.
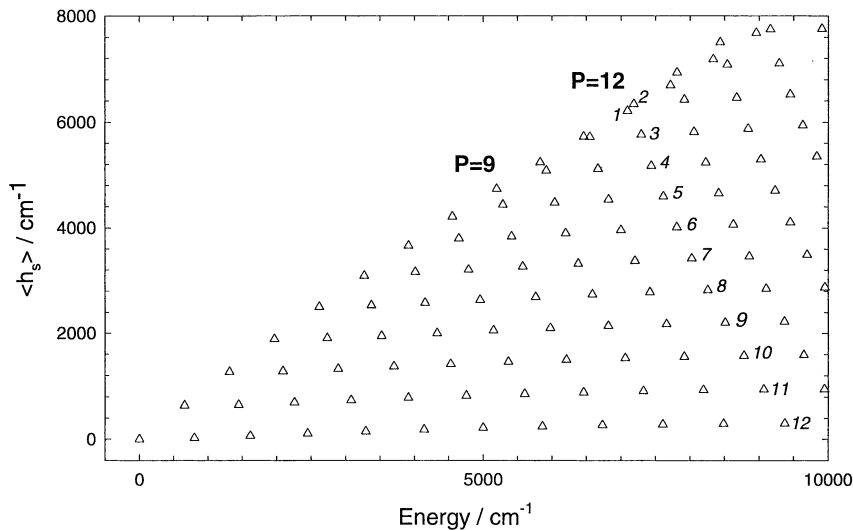
Fig. 8. Expectation values of $\langle \hat{h}_s \rangle$, calculated from spectroscopic fitting Hamiltonian as discussed in connection with Eq. (12). The levels of polyad 12 are numbered as on the phase sphere in Fig. 7.

known example is probably the birth of local modes in a bifurcation from one of the normal modes [38,77]. The overall bifurcation structure can be neatly described using a tool of bifurcation analysis known as the catastrophe map, adapted to molecular spectroscopy [28,72]. Fig. 9 shows a portion of the catastrophe map for the 1:2 Fermi resonance. Each polyad is represented by a point on the map. Fig. 9 shows the polyads of CS_2, and also of CO_2, which offers an illuminating comparison, which we will take up after discussing the semiclassical analysis of CS_2. The map shows that polyads 1 and 2 of CS_2 lie in Zone I and the remaining polyads in Zone II. Briefly, the meaning of these zones is the following [28]. In Zone I there are normal stretching and bending modes; in Zone II, a bifurcation has taken place in which the north pole becomes a cusp, signaling the onset of instability in the symmetric stretch. A new stable mode is formed, displaced from the original north pole. The effects are evident in the phase sphere of Fig. 7. In coordinate space, this new mode has the shape of a hairpin. Not surprisingly, this will turn out to be closely related to the 'hairpin' wave function (9, 0, 0) in Fig. 6: the ride of the wave function follows the underlying hairpin mode, a well-known phenomenon, see Ref.

[72]. This new mode born in the bifurcation of the symmetric stretch is closely related to the kinks in Figs. 8 and 5 (top). For example, in Fig. 8, levels 1 and 2, which form the kink of polyad $P = 12$, are the levels most affected by the bifurcation on the sphere in Fig. 7.
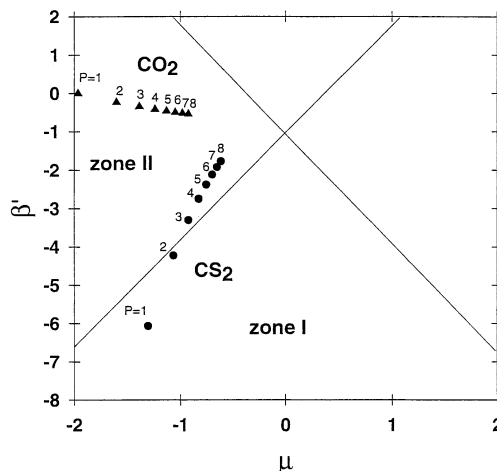

Fig. 9. Catastrophe map classifications of polyads of CS_2 (circles) and CO_2 (triangles). Each polyad with its phase sphere is represented by a point on the map. The coordinates are a scaled Fermi coupling strength μ and asymmetry parameter β' (related to the zero-order normal mode frequencies). See Ref. [28]. for detailed exposition of the catastrophe map.

We claim in fact that the cusp bifurcation and transition from normal mode (Zone I) dynamics to resonant (Zone II) dynamics accounts for all of the anomalies we have noted: the kinks in Fig. 5 starting at about $P = 9$, the marbled appearance of the phase sphere in Fig. 7, and the hairpin wave function of Fig. 6 for the state labeled (9, 0, 0). But, in the catastrophe map of Fig. 9, the bifurcation to Zone II dynamics actually begins with $P = 3$. Then why donot the effects of the bifurcation show up until $P = 9$?

To answer this, and to further establish the comprehensive role of bifurcation phenomena in understanding all the anomalies, we make use of the pseudo-potential [80–82], a technique used in the bifurcation analysis which is also extremely useful as an interpretive tool. The pseudo-potential originates from the fact that the bifurcations of the polyad Hamiltonian all occur on a single great circle on the phase sphere [38] [78]. The bifurcation analysis is therefore performed by analyzing the Hamiltonian plotted just on this great circle. This is the pseudo-potential. The critical points of the pseudo-potential—maxima, minima, and points of inflection—give the periodic orbits, that is to say anharmonic modes of the system: the normal modes, and the new modes born in bifurcations.

Fig. 10 shows the pseudo-potentials for polyads 2, 5, 9, and 12. For $P = 2$ there are two critical points, labeled **s** and **b** corresponding to the symmetric stretch and the bend. No bifurcation has yet taken place. At $P = 5$ a very small maximum has developed at the north pole, and the minimum formerly at the north pole has been slightly displaced. This signals the onset of the cusp bifurcation (which actually has occurred by $P = 3$, as indicated on the catastrophe map, but the minimum in the $P = 3$ pseudo-potential is imperceptible) in which the stretch (north pole) becomes unstable, and a new stable mode (resonant hairpin mode, labeled **h** in Fig. 10) is born, and immediately starts to be displaced from the north pole. (The bend, which has not bifurcated, is very slightly displaced from its zero-order position at the south pole.)

This bifurcation still does not produce at $P = 5$ either the kinks in Figs. 5 and 8 or the hairpin

wave function for the state labeled (9, 0, 0) in Fig. 6. The reason why can be seen by plotting the quantum energy levels in the pseudo-potential. At $P = 5$, the lowest level is still above the tiny minimum formed in the pseudo-potential when the bifurcation takes place. In contrast, by $P = 9$, the lowest level is 'trapped' in the minimum—which corresponds to the resonant hairpin orbit. This is reflected in the kink for $P = 9$ in Figs. 5 and 8: the lowest energy level 1 has less symmetric stretching character than level 2, because level 1 is trapped in the resonant minimum, away from the north pole. The trapping of level 1 is also reflected in the hairpin shape of the wave function labeled (9, 0, 0) in Fig. 6. Finally, the pseudo-potential for $P = 12$ casts further light on the phase sphere of Fig. 7 and the kink of $P = 12$ in Figs. 5 and 8. Level 1 is trapped in the minimum corresponding to the hairpin mode; level 2 touches the 'lip' of the well. This is reflected perfectly on the sphere, Fig. 7, and the kink in Figs. 5 and 8 with the lesser symmetric stretch content of level 1.

The appearance of bifurcations of the normal modes and the existence of wave functions such as the hairpin state assigned (9, 0, 0) in Fig. 6 raises the questions whether a normal mode assignment is really appropriate at all for a molecule like CS_2. Two of the present authors have argued [72,82,83] that in resonant systems, a new assignment should be used, with quantum numbers suited to the new modes born in the bifurcations; and that this new assignment is reflected in the phase spheres, catastrophe map analysis, and new types of spectral patterns. In fact, an alternative assignment to that of the normal mode assignment for CS_2 made here can be carried out, and does show the predicted [83] associated spectral patterns. However, we do not pursue this, for reasons we will now discuss, which also involve some illuminating differences between CS_2 and CO_2 as regards their polyads classified on the catastrophe map.

In the catastrophe map of Fig. 9 the polyads of CS_2 straddle the boundary of Zones I and II in Fig. 9, whereas those of CO_2 are firmly in Zone II. This suggests that CS_2 is only weakly influenced by the 1:2 Fermi resonance. This is reflected in the fact that the phase sphere of Fig. 7 is affected by the bifurcation, but mainly near the
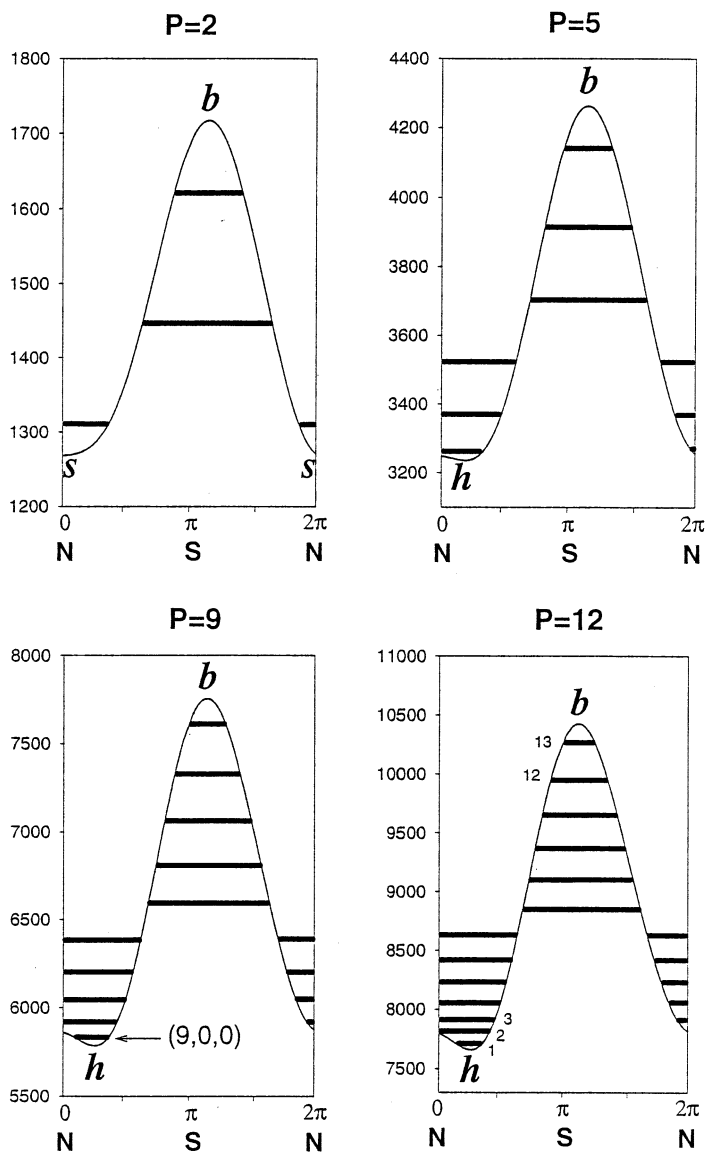
Fig. 10. Pseudo-potentials for polyads 2, 5, 9 and 12. The individual quantum levels are indicated. The x-axis is the angle on the 'great circle of bifurcations' of the phase sphere [38], with north and south pole indicated; y-axis is energy in cm^{-1}. The symmetric stretch **s**, hairpin mode **h**, and bend **b** are indicated. See Ref. [82] for details of the pseudo-potential method.

north pole; and in the weak effects of the Fermi resonance seen in the pseudo-potentials of Fig. 10. We can say that CS_2 is only weakly, or even just barely, a Fermi resonance molecule. A new assignment based on the bifurcation analysis would be proper, but not more illuminating than what has already been said here, e.g. about the hairpin

state assigned conventionally as $(9, 0, 0)$. In contrast, CO_2 displays strongly resonant dynamics as clearly reflected in its phase spheres, spectral patterns, wave functions, and quantum number assignments, as discussed in Ref. [83]. The difference is due to the fact that in CO_2, there is a very close 1:2 resonance in the zero-order stretch

and bend frequencies. This is reflected in the catastrophe map, Fig. 9, where it is seen that for CO_2, all the polyads have nearly zero asymmetry parameter β'. The result is that the Fermi resonance dominates the vibrational dynamics in CO_2, with a profound reorganization of the phase space.

This is about as far as we can go in extracting meaning from the effective Fermi resonance Hamiltonian of Section 3.1 by means of semiclassical analysis. The more disordered spectra that set in at about 12,000 cm^{-1}, as well as a few of the lower-lying levels as discussed above, require a multiresonance Hamiltonian, corresponding to chaotic classical dynamics, to get a good fit to the detailed levels. When such an effective Hamiltonian is available, there are now methods for classifying patterns even of spectra, which are significantly influenced by chaos [73–75].

4. Summary

In this study, we have developed an empirical PES for $CS_2(\tilde{X})$ by fitting experimental vibrational band origins below 6000 cm^{-1}. The properties of the potential, such as force constants, are in good agreement with known values obtained from previous spectroscopic and ab initio work. Low-lying ro-vibrational energies for CS_2 ($l = 0.1$) and those for three isotopic substitutions $^{13}CS_2$, $^{33}SC^{32}S$ and $^{34}SC^{32}S$ were obtained from this PES and found in good experiment with experimental values. This PES was then used to calculate highly excited vibrational spectrum of CS_2 up to 20,000 cm^{-1}, using PODVRs in the symmeterized Radau coordinates and the Lanczos algorithm. A total of 2339 vibrational levels have been identified. Statistical analysis indicated the CS_2 vibrational spectrum in this energy range is largely regular, consistent with the latest experimental data. It was shown that normal mode assignment can be readily made for low-lying levels with the help of the expectation values of 1D reference Hamiltonians. The antisymmetric stretching mode is effectively decoupled from the remaining two modes up to 15,000 cm^{-1}. A spectroscopic fitting Hamiltonian with 1:2 Fermi resonance coupling was constructed by fitting the calculated spectra up to the energy where multiple resonances begin to affect the spectrum. Despite strong intermodal coupling between the symmetric stretching and bending modes, no strong intra-polyad Fermi and anharmonic resonances were found to increase with the density of states. Detailed analysis shows that some subtle anomalies are signaled by the detailed tools used to make the normal modes assignment, specifically, the normal modes quantum content of the states. These anomalies are interpreted in terms of semiclassical analysis, including bifurcation analysis of a semiclassical version of the spectroscopic fitting Hamiltonian. This accounts for the anomalies, and also some subtle incongruous patterns in some wave functions, in terms of a bifurcation of the symmetric stretching mode, which takes place due to the Fermi coupling. However, the molecular phase space is only weakly affected by this bifurcation. This clarifies the meaning of 'Fermi resonance', by the contrast with CO_2, where the close 1:2 resonance in the zero-order stretching and bending frequencies means that the Fermi coupling dominates the vibrational dynamics, with massive reorganization of the semiclassical phase space and the structure of wave functions.

References

[1] Q. Zhang, P.H. Vaccaro, J. Phys. Chem. 99 (1995) 1799.
[2] S.T. Brown, T.J.V. Huis, B.C. Hoffman, H.F. Schaefer, Mol. Phys. 96 (1999) 693.
[3] G. Blanquet, E. Baeten, I. Cauet, J. Walrand, C.P. Courtoy, J. Mol. Spectrosc. 112 (1985) 55.
[4] J. Lindenmayer, H. Jones, J. Mol. Spectrosc. 110 (1985) 65.

[5] J. Walrand, V. Humblet, G. Blanquet, J. Mol. Spectosc. 127 (1988) 304.

[6] C.-L.C. Cheng, J.L. Hardwick, T.R. Dyke, J. Mol. Spectrosc. 179 (1996) 205.

[7] J. Walrand, G. Blanquet, J.-F. Blavier, H. Bredohl, I. Dubois, Mol. Phys. 89 (1996) 1145.

[8] P.F. Bernath, M. Dulick, R.W. Field, J.L. Harwick, J. Mol. Spectrosc. 86 (1981) 275.

[9] H. Kasahara, N. Mikami, M. Ito, S. Iwata, I. Suzuki, Chem. Phys. 86 (1984) 173.

[10] R.A. Desiderio, D.P. Gerrity, B.S. Hudson, Chem. Phys. Lett. 115 (1984) 29.

[11] J.P. Pique, J. Manners, G. Sitja, M. Joyeux, J. Chem. Phys. 96 (1992) 6495.

[12] G. Sitja, J.P. Pique, Phys. Rev. Lett. 73 (1994) 232.

[13] G. Brasen, W. Demtröder, J. Chem. Phys. 110 (1999) 11 841.

[14] Q. Zhang, S.A. Kandel, T.A.W. Wasserman, P.H. Vaccaro, J. Chem. Phys. 96 (1991) 1640.

[15] H.T. Liou, P. Dan, H. Yang, J.-Y. Yuh, Chem. Phys. Lett. 176 (1991) 109.

[16] H.T. Liou, K.L. Huang, Chem. Phys. 246 (1999) 391.

[17] A.G. Maki, J. Mol. Spectrosc. 47 (1973) 217.

[18] A.G. Maki, R.L. Sams, J. Mol. Spectrosc. 52 (1974) 233.

[19] L.S. Masukidi, J.G. Lahaye, A. Fayt, J. Mol. Spectrosc. 148 (1991) 281.

[20] T. Platz, M. Matheis, C. Hornberger, W. Demtröder, J. Mol. Spectrosc. 180 (1996) 81.

[21] L. Michaille, U. Rasbach, J.P. Pique, J. Chem. Phys. 111 (1999) 2968.

[22] D.F. Smith, J. Overend, J. Chem. Phys. 54 (1971) 3632.

[23] I. Suzuki, Bull. Chem. Soc. Jpn. 48 (1975) 1685.

[24] M. Lacy, D.H. Whiffen, Mol. Phys. 43 (1981) 1205.

[25] E. Fermi, Z. Phys. 71 (1931) 250.

[26] E.J. Heller, E.B. Stechel, M.J. Davis, J. Chem. Phys. 73 (1980) 4720.

[27] E.L. Sibert, J. Hynes, W.P. Reinhardt, J. Phys. Chem. 87 (1983) 2032.

[28] L. Xiao, M.E. Kellman, J. Chem. Phys. 93 (1990) 5805.

[29] G. Herzberg, Molecular spectra and molecular structure, in: Infrared and Raman Spectra of Polyatomic Molecules, vol. 2, Van Nostrand, Princeton, 1945.

[30] J.P. Pique, M. Joyeux, J. Manners, G. Sitja, J. Chem. Phys. 95 (1991) 8744.

[31] M. Joyeux, J. Mol. Spectrosc. 175 (1996) 262.

[32] J.N. Murrell, H. Guo, J. Chem. Soc. Faraday Trans. II 83 (1987) 683.

[33] M. Kolbuszewski, P.R. Bunker, P. Jensen, J. Mol. Spectrosc. 170 (1995) 158.

[34] J. Zuniga, A. Bastida, M. Alacid, A. Requena, Chem. Phys. Lett. 313 (1999) 670.

[35] J.M.L. Martin, J.-P. Francois, R. Gijbels, J. Mol. Spectrosc. 169 (1995) 445.

[36] M.E. Kellman, E.D. Lynch, J. Chem. Phys. 85 (1986) 7216.

[37] L. Xiao, M.E. Kellman, J. Chem. Phys. 90 (1989) 6086.

[38] Z. Li, L. Xiao, M.E. Kellman, J. Chem. Phys. 92 (1990) 2251.

[39] M. Joyeux, Chem. Phys. 185 (1994) 263.

[40] M. Joyeux, Chem. Phys. 203 (1996) 281.

[41] A.B. Myers, B. Li, X. Ci, J. Chem. Phys. 89 (1982) 1876.

[42] M.F. Arendt, L.J. Butler, J. Chem. Phys. 109 (1998) 7835.

[43] A. McNichols, T. Carrington, Chem. Phys. Lett. 202 (1993) 464.

[44] M.J. Bramley, T. Carrington, J. Chem. Phys. 99 (1993) 8519.

[45] V.A. Mandelshtam, T.P. Grozdanov, H.S. Taylor, J. Chem. Phys. 103 (1995) 10 074.

[46] S. Skokov, J. Qi, J.M. Bowman, C.-Y. Yang, S.K. Gray, K.A. Peterson, V.A. Mandelshtam, J. Chem. Phys. 109 (1998) 10 273.

[47] F. Gatti, C. Iung, C. Leforestier, X. Chapuisat, J. Chem. Phys. 111 (1999) 7236.

[48] R. Chen, H. Guo, Chem. Phys. Lett. 277 (1997) 199.

[49] G. Ma, H. Guo, J. Chem. Phys. 111 (1999) 4032.

[50] R. Chen, G. Ma, H. Guo, Chem. Phys. Lett. 320 (2000) 567.

[51] J.C. Light, I.P. Hamilton, J.V. Lill, J. Chem. Phys. 82 (1985) 1400.

[52] G. Yan, D. Xie, A. Tian, J. Phys. Chem. 98 (1994) 8870.

[53] G.D. Carney, L.L. Sprandel, C.W. Kern, Adv. Chem. Phys. 37 (1978) 305.

[54] C. Lanczos, J. Res. Natl. Bur. Stand. 45 (1950) 255.

[55] J.K. Cullum, R.A. Willoughby, Lanczos Algorithms for Large Symmetric Eigenvalue Computations, Birkhauser, Boston, 1985.

[56] B.R. Johnson, W.P. Reinhardt, J. Chem. Phys. 85 (1986) 4538.

[57] J. Echave, D.C. Clary, Chem. Phys. Lett. 190 (1992) 225.

[58] H. Wei, T. Carrington, J. Chem. Phys. 97 (1992) 3029.

[59] D.T. Colbert, W.H. Miller, J. Chem. Phys. 96 (1992) 1982.

[60] M.J. Bramley, J.W. Tromp, T. Carrington, G.C. Corey, J. Chem. Phys. 100 (1994) 6175.

[61] G.C. Corey, J.W. Tromp, D. Lemoine, in: C. Cerjan (Ed.), Numerical Grid Methods and their Applications to Schrödinger's Equation, Kluwer, Dordrecht, 1993.

[62] R. Chen, H. Guo, J. Chem. Phys. 111 (1999) 9944.

[63] R. Chen, H. Guo, Chem. Phys. Lett. 308 (1999) 123.

[64] R. Chen, H. Guo, J. Chem. Phys. 114 (2001) 1467.

[65] G.Z. Whitten, B.S. Rabinovitch, J. Chem. Phys. 38 (1963) 2466.

[66] T.A. Brody, J. Flores, J.B. French, P.A. Mello, A. Pandey, S.S.M. Wong, Rev. Mod. Phys. 53 (1981) 385.

[67] T. Zimmerman, L.S. Cederbaum, H.-D. Meyer, H. Köppel, J. Phys. Chem. 91 (1987) 4446.

[68] E.P. Wigner, SIAM Rev. 1 (1967) 1.

[69] M.V. Berry, M. Tabor, Proc. Royal Soc. London Ser. A. 356 (1979) 375.

[70] F.J. Dyson, M.L. Mehta, J. Math. Phys. 4 (1963) 701.

[71] E. Haller, H. Köppel, L.S. Cederbaum, Chem. Phys. Lett. 101 (1983) 215.

[72] M.E. Kellman, L. Xiao, J. Chem. Phys. 93 (1990) 5821.

[73] J.P. Rose, M.E. Kellman, J. Chem. Phys. 105 (1996) 7348.

[74] J.P. Rose, M.E. Kellman, J. Phys. Chem. A104 (2000) 10 471.

[75] M.E. Kellman, J.P. Rose, V. Tyng, Euro. Phys. H. D (2001).

[76] M.E. Kellman, in: Encyclopedia of Chemical Physics and Physical Chemistry, Institute of Physics, in press.

[77] M.E. Kellman, Annu. Rev. Phys. Chem. 46 (1995) 395.

[78] M.E. Kellman, in: H.-L. Dai, R.W. Field (Eds.), Molecular Dynamics and Spectroscopy by Stimulated Emission Pumping, World Scientific, Singapore, 1995.

[79] A. Vardi, J.R. Anglin, Phys. Rev. Lett. 86 (2001) 568.

[80] L. Xiao, PhD Thesis, Northeastern University, 1991.

[81] J.F. Svitak, PhD Thesis, University of Oregon, 1998.

[82] M. Joyeux, D. Sugny, B. Tyng, M.E. Kellman, R.W. Field, C. Beck, R. Schinke, J. Chem. Phys. 112 (2000) 4162.

[83] J. Svitak, Z. Li, J. Rose, M.E. Kellman, J. Chem. Phys. 102 (1995) 4340.